Atmos. Meas. Tech. Discuss., 5, 163–210, 2012
www.atmos-meas-tech-discuss.net/5/163/2012/
doi:10.5194/amtd-5-163-2012

Atmospheric Measurement Techniques Discussions

Filling-in of far-red and near-Infrared solar lines by terrestrial and atmospheric effects: simulations and space-based observations from SCIAMACHY and GOSAT

J. Joiner[1], Y. Yoshida[2], A. P. Vasilkov[2], E. M. Middleton[1], P. K. E. Campbell[3], Y. Yoshida[4], A. Kuze[5], and L. A. Corp[6]

[1]NASA Goddard Space Flight Center, Greenbelt, MD, USA
[2]Science Systems and Applications, Inc., 10210 Greenbelt, Rd., Ste 400, Lanham, MD, USA
[3]University of Maryland, Baltimore County, Joint Center for Environmental Technology (UMBC-JCET), Baltimore, MD, USA
[4]National Institute for Environmental Studies (NIES), Tsukuba-City, Ibaraki, Japan

[5]Japan Aerospace Exploration Agency (JAXA), Tsukuba-City, Ibaraki, Japan
[6]Sigma Space Corp., Lanham, MD USA

Received: 19 October 2010 – Accepted: 28 October 2010 – Published: 6 January 2012

Correspondence to: J. Joiner (joanna.joiner@nasa.gov)

Published by Copernicus Publications on behalf of the European Geosciences Union.

Abstract

Global mapping of terrestrial vegetation fluorescence from space has recently been accomplished with high spectral resolution ($\nu/\Delta\nu > 35\,000$) measurements from the Japanese Greenhouse gases Observing SATellite (GOSAT). These data are of interest because they can potentially provide global information on the functional status of vegetation including light use efficiency and global primary productivity that can be used for global carbon cycle modeling. Quantifying the impact of fluorescence on the O_2-A band is important as this band is used for cloud- and aerosol-characterization for other trace-gas retrievals including CO_2. Here, we explore whether fluorescence information can be derived from space using potentially lower-cost hyperspectral instrumentation, i.e., more than an order of magnitude less spectral resolution ($\nu/\Delta\nu \sim 1600$) than GOSAT, with a relatively simple algorithm. We simulate the filling-in, from various atmospheric and terrestrial effects, of one of the few wide and deep solar Fraunhofer lines in the long-wave tail of the fluorescence emission region, the calcium (Ca) II line near 866 nm. We then examine filling-in of this line using the SCanning Imaging Absorption spectroMeter for Atmospheric CHartographY (SCIAMACHY) satellite instrument. We develop and apply methodology to correct for various instrumental artifacts that produce false filling-in of solar lines in satellite radiance measurements. We then compare the derived additive near-InfraRed (NIR) signal at 866 nm, that fills in the Ca II line, with larger signals retrieved at 758 and 770 nm on the shoulders of the O_2-A feature from GOSAT that are presumably due primarily to vegetation fluorescence. Finally, we compare temporal and spatial variations of GOSAT and SCIAMACHY additive signals with those of the Enhanced Vegetation Index (EVI) from the MODerate-resolution Imaging Spectroradiometer (MODIS). Although the observed filling-in signal from SCIAMACHY is extremely weak at 866 nm, the spatial and temporal patterns of the derived additive signal are consistent with a vegetation source, chlorophyll-a fluorescence being a plausible candidate. We also show that filling-in occurs at 866 nm over some barren areas, possibly originating from luminescent minerals in rock and soil.

AMTD
5, 163–210, 2012

1 Introduction

Fluorescence from terrestrial vegetation has been measured in the laboratory and with ground- and aircraft-based instruments for several decades (see e.g., the review of Meroni et al., 2009, and the many references therein). More recently, it has been demonstrated that fluorescence information can also be derived from satellite passive sensors measuring backscattered sunlight at wavelengths near the O_2-A band absorption feature. These fluorescence measurements, particularly with global coverage from satellites, are of interest because the signal originates from the core complexes of the photosynthetic machinery where energy conversion of absorbed photosynthetically active radiation (PAR) occurs. Chlorophyll fluorescence measurements therefore may provide a means to estimate global instantaneous vegetation carbon-related processes. These processes are of major interest for precision farming, forest management, and assessment of the terrestrial carbon budget including gross primary productivity (GPP) (e.g., Campbell et al., 2008; Damm et al., 2010; Frankenberg et al., 2011b). In addition, it is important to quantify the impact of fluorescence on atmospheric absorption bands, such as the O_2-A band, that are used for cloud- and aerosol-characterization for other trace-gas retrievals, including CO_2 (e.g., Frankenberg et al., 2011a).

Fluorescence in vegetation occurs because a portion of the sunlight absorbed by chlorophyll cannot be used for carbon fixation. While most of this unused energy is given off as heat, a small fraction is re-emitted as fluorescence at longer wavelengths (lower energy) with respect to the excitation wavelength. The far-red and red fluorescence generally occurs as a convolution of broad band emission with two peaks at 685 and 740 nm, respectively, as shown in Fig. 1 (e.g., Meroni et al., 2009; Corp et al., 2003, 2006). Many studies have shown that in high light conditions (i.e., in the late morning and early afternoon when many satellite measurements are made) and when plants are under stress, fluorescence is correlated with photosynthesis and light use efficiency (LUE) (e.g., Flexas et al., 2002; Louis et al., 2005; Meroni et al., 2008; van

AMTD
5, 163–210, 2012

der Tol et al., 2009; Zarco-Tejada et al., 2009; Daumard et al., 2010; Amoros–Lopez et al., 2008). Other research has indicated that chlorophyll fluorescence supplies information content about photosynthetic function that is complementary to reflectance-based spectral vegetation indices including the Normalized Difference Vegetation Index (NDVI) and the Enhanced Vegetation Index (EVI) linked to chlorophyll content, and the Photochemical Reflectance Index (PRI) related to changes in xanthophyll cycle pigments (Meroni and Colombo, 2006; Middleton et al., 2008, 2009; Rascher et al., 2009; Meroni et al., 2008; Daumard et al., 2010; Guanter et al., 2007; Zarco-Tejada et al., 2009; Joiner et al., 2011a; Frankenberg et al., 2011b).

Space-based measurement of solar-induced chlorophyll fluorescence is challenging, because its signal (typically 1–5 % at red and far-red wavelengths) is small as compared with the much larger reflectance signal. Ground- and aircraft-based approaches have made use of the dark and spectrally-wide O_2-A (~760 nm) and O_2-B (~690 nm) atmospheric features to detect the weak fluorescence signal (see e.g., Meroni et al., 2009). Deep solar Fraunhofer lines have also been used to detect fluorescence from vegetation using airborne and ground-based sensors. Initial studies (e.g., Plascyk and Gabriel, 1975; McFarlane et al., 1980; Watson, 1981; Sioris et al., 2003) focused on lines shortward of the red edge (~700 nm) where the terrestrial surface albedo is relatively low. More recently, Joiner et al. (2011a) and Frankenberg et al. (2011a,b) focused on longer-wavelength solar Fraunhofer lines that can be observed with space-based instruments such as the currently operational GOSAT. They showed that fluorescence can be detected using Fraunhofer lines away from the far-red chlorophyll-a fluorescence peak even when the surface is relatively bright.

Here, we build on that work by developing methodology to correct for instrumental artifacts that produce false filling-in signals that can bias fluorescence retrievals. We also examine other potential sources of filling-in at far-red and NIR wavelengths. In addition to vegetation, minerals in rocks and soil may luminesce from blue to far-red or NIR wavelengths and contribute to the filling-in of Fraunhofer lines. Mineral detection was a primary goal of early measurements using the Fraunhofer line discriminator

AMTD
5, 163–210, 2012

method (e.g., Hemphill and Vickers, 1966; Watson, 1981; Stacy et al., 1984; Hemphill et al., 1988). Another objective is to explore the possibility of making fluorescence measurements from space with lower spectral resolution instrumentation than the GOSAT interferometer. If this can be demonstrated, then low cost instrumentation can potentially be used for such measurements with a relatively simple retrieval algorithm, i.e., one that does not require complex atmospheric correction.

Of the wide and deep solar lines shown in Fig. 1, we focus on the 866 nm Ca II solar Fraunhofer line. This is the only line with negligible contamination from atmospheric water vapor capable of detecting fluorescence at spectral resolutions of about 0.5 nm. We simulate the potential filling-in of this line from atmospheric effects, namely vibrational and rotational Raman scattering, as well as from fluorescence and high temperature emitters such as fires and volcanoes. We then make use of unique spectral radiance measurements from the SCanning Imaging Absorption spectroMeter for Atmospheric CHartographY (SCIAMACHY) instrument aboard the European Space Agency (ESA) Environmental satellite (EnviSat) encompassing the Ca II line at 866 nm. SCIAMACHY observations are used to retrieve an additive signal that fills in the Ca II line. These measurements are at the long wavelength tail of the chlorophyll-a fluorescence spectrum. This is clearly not an optimal wavelength region for measuring fluorescence owing to the extreme weakness of the signal; instrumental artifacts could easily overwhelm a fluorescence signal. Though not optimized for detecting fluorescence, SCIAMACHY can be used for an exploratory study.

The paper is organized as follows: we discuss laboratory measurements of fluorescence at the long-wavelength tail of the chlorophyll-a fluorescence spectrum in Sect. 2. Section 3 describes the satellite observations used here. Simulations of the Ca II line-filling at 866 nm from atmospheric rotational- and vibrational-Raman scattering as well as fluorescence are given in Sect. 4. The details of our retrieval approach, including methodology to correct for instrumental artifacts, are provided in Sect. 5. We show maps of monthly-mean derived additive signals from 866 nm Ca II line-filling and a seasonal climatology using more than 8 yr of SCIAMACHY data in Sect. 6. In this section,

AMTD
5, 163–210, 2012

we also compare and contrast temporal and spatial variations of the additive signals (retrieved from both SCIAMACHY and GOSAT) with the MODIS EVI. Conclusions are given in Sect. 7.

2 Laboratory measurements

Very few laboratory and ground-based measurements of vegetation fluorescence have been reported at wavelengths longer than 800 nm. Figure 1 displays fluorescence measurements of corn leaves acquired in the laboratory using polychromatic excitation at wavelengths shorter than 665 nm (Oriel 91160A and Oriel 81080) after a five minute dark adaptation of the samples as described in Campbell et al. (2008). Chlorophyll fluorescence levels decrease significantly from the initial dark-adapted maximum (F_{max}) to the steady state (F_s) in 15–20 s, after which they remain relatively constant over time. Here, we show that F_{max} and F_s in the red and far-red peaks vary significantly, but are much lower in value and do not differ significantly in the emission tails (e.g., at 656 and 854–866 nm). At 866 nm, the measured signal is of the order of 0.1–0.2 mW m^{-2} nm^{-1} sr^{-1}.

Amoros–Lopez et al. (2008) similarly report spectral measurements from 650–850 nm showing a small amount of fluorescence (~0.1 mW m^{-2} nm^{-1} sr^{-1}) at 850 nm when illuminated by sunlight through a filter that restricts excitation to wavelengths shorter than about 600 nm (i.e., not full ambient intensity at leaf level). Other measurements (e.g., Chappelle and Williams, 1987; Rosema et al., 1991; Edner et al., 1994; Saito et al., 1998) suggest that the long-wave tail of the chlorophyll-a fluorescence emissions and perhaps fluorescence from other compounds such as vitamin K_1 (Chappelle et al., 1984) may produce a measurable signal at wavelengths beyond 800 nm.

We did not, however, detect a resolvable fluorescence signal with respect to instrument signal-to-noise at 866 nm using a Fluorolog® 3 spectrofluorometer with monochromatic excitation. Excitation wavelengths ranging from the ultraviolet through the visible were used. One possible explanation is that fluorescence at the long

AMTD
5, 163–210, 2012

wavelength tail of the fluorescence spectrum may be higher when induced by full-spectrum sunlight as compared with a monochromatic source or in a partially-illuminated scenario. Measurements have shown that the excitation efficiency of chlorophyll fluorescence is high in the blue and ultraviolet (UV) with a minimum around 550 nm and another peak of high efficiency beyond about 650 nm (Chappelle and Williams, 1987; Rosema et al., 1991; Middleton et al., 2008).

3 Satellite observations

3.1 SCIAMACHY

SCIAMACHY is a grating spectrometer that measures transmitted, reflected, and scattered sunlight in both limb- and nadir-viewing geometries from ultraviolet to near-infrared wavelengths (212–2386 nm) in eight separate channels. It was launched on the EnviSat platform in February 2002 into a sunsynchronous orbit with a descending node equator crossing time near 10:00 LT. The instrument can make measurements in a number of different modes (e.g., Lichtenberg et al., 2006). In addition to Earth views in the limb and nadir, it can operate in a solar or lunar occultation mode. It also measures the solar irradiance. In this work, we primarily use channel 5 that covers wavelengths between 773 and 1063 nm at a spectral resolution of 0.54 nm. The signal-to-noise ratio for nadir measurements in this channel is between 1000 and 10 000 (Gottwalk et al., 2006) and the ground footprint size is approximately 30 km in the along track direction and about 60 km in the cross-track direction for latitudes between 60° N and 60° S. We also examined spectra in channel 4 that covers 595–812 nm at 0.48 nm spectral resolution.

We processed raw SCIAMACHY level 1B data with the SciaL1c command-line tool software package (DLR, 2006). Using this package, we applied all available corrections and calibrations. Although the corrections do an excellent job of removing most artifacts that produce false filling-in of solar Fraunhofer lines, we found it necessary to further

AMTD
5, 163–210, 2012

account for the remaining effects as discussed in Sect. 5. In Appendix A, we give a brief overview of the effects. More details can be found in Lichtenberg et al. (2006).

3.2 GOSAT

GOSAT is a satellite mission designed to monitor the global distribution of the greenhouse gases CO_2 and CH_4 (Yokota et al., 2009). Jointly developed by the Japanese Ministry of the Environment (MOE), the National Institute for Environmental Studies (NIES), and the Japanese Aerospace Exploration Agency (JAXA), GOSAT was launched on 23 January 2009 into a sun-synchronous orbit. It has a descending node equatorial crossing time near 13:00 LT and a 3 day repeat cycle. GOSAT has two instrument packages: (1) the Thermal And Near-infrared Sensor for carbon Observation-Fourier Transform Spectrometer (TANSO-FTS) (Kuze et al., 2009) measures backscattered solar radiation in three shortwave infrared (SWIR) regions, referred to as "bands", centered at 0.76, 1.6, and 2.0 µm with a nadir ground footprint of 10.5 km diameter and (2) the Cloud and Aerosol Imager (CAI) contains four bands at 0.38, 0.67, 0.87, and 1.6 µm and footprints between 0.5 and 1.5 km.

Joiner et al. (2011a) and Frankenberg et al. (2011b) retrieved chlorophyll fluorescence using TANSO-FTS band 1. This band extends from approximately 758 to 775 nm with a resolving power ($\nu/\Delta\nu$) of >35 000. The signal-to-noise ratio (SNR) for this band is >300 for a typical scene radiance.

There are also instrumental effects that can distort GOSAT spectra to produce a false filling-in of Fraunhofer lines. These include non-linearity from the analog-to-digital converter (ADC) (Kuze et al., 2011b) and the analog filter circuit in band 1 that can lead to effects such as a zero-level offset (Frankenberg et al., 2011b). In addition, calibration drift (Kuze et al., 2011a) may produce errors and drift in the absolute values of the derived additive signal. The latest available version (v130) of the level 1b data addresses some, but not all of these problems. Future versions will provide more corrections for these non-linearities. Only a limited amount of v130 data is currently available. Therefore, here we use a previous version of level 1b data (v050-v100)

AMTD
5, 163–210, 2012

with an approach to account for instrumental artifacts that produce false filling in as described below.

3.3 MODIS Vegetation indices

Below, we compare satellite-derived fluorescence with the Enhanced Vegetation Index (EVI) (Huete et al., 2002), a popular vegetation reflectance-based index that indicates relative greenness and is used to infer photosynthetic function. The EVI, derived from the MODIS instrument, can be found in the "Vegetation Indices 16-Day L3 Global 1 km" (MOD13A2) data set. We use data from the Aqua MODIS, acquired in the early afternoon, exclusively here for direct comparisons with 2009 GOSAT results and averaged over the period August 2002 through June 2011 for climatological comparisons with SCIAMACHY. The Aqua satellite has an ascending node equator crossing near 13:30 LT. Although these data have been cloud-filtered and corrected for aerosol-corruption effects, we followed the methodology of Xu et al. (2011) to further remove residual atmospheric corruption in order to produce the best possible signals from vegetation.

4 Simulated filling-in at 866 nm

Here, we simulate the effects of additive signals such as fluorescence as well as rotational- and vibration-Raman scattering on space-based observations of the Ca II line near 866 nm. We use the so-called KPNO2010 high spectral resolution solar irradiance reference spectrum (Chance and Kurucz, 2010) for these simulations and convolve the spectrum with triangular instrument line shape functions having different values of the full-width half-maximum (FWHM) including one similar to SCIAMACHY.

AMTD
5, 163–210, 2012

4.1 Fluorescence and other additive signals

Figure 2 shows simulated filling-in of the 866 nm Ca II solar line for a spectrally constant additive signal of 0.2 mW m^{-2} sr^{-1} nm^{-1}, for several different spectral resolutions including the limit at monochromatic resolution. Because Rayleigh optical thickness is low at these wavelengths, we did not include atmospheric scattering in these simulations. The filling-in at SCIAMACHY resolution is small (<1 %). However, modest increases in spectral resolution will increase the filling-in.

Figure 3 shows the surface-albedo dependence of the simulated filling-in of the 866 nm Ca II line for the same signal (0.2 mW m^{-2} nm^{-1} sr^{-1}) and spectral resolutions as in Fig. 2. The surface albedo dependence is significant at low surface albedos. However, the dependence flattens out at values typical of vegetated land (>∼0.25).

Note that we make no assumption here about the source of the additive signal. Fluorescence from vegetation or minerals is one possible source. Another such source is radiation from fires or volcanoes. Using the Planck function, we estimate that the radiance from a source at 1000 K will produce a signal of the order of 15 mW m^{-2} nm^{-1} sr^{-1} at 866 nm and ∼3 mW m^{-2} nm^{-1} sr^{-1} at 770 nm. If such a source filled a SCIAMACHY or GOSAT field-of-view, it would certainly be detectable. However, flaming portions of fires and sources of hot gas and lava from volcanoes are most likely to fill only a small fraction of the relatively large GOSAT or SCIAMACHY footprints. Never-the-less, fires and volcanoes should be considered as potential sources of solar line filling at far-red and NIR wavelengths. Reducing temperatures to <∼650 K renders the filling-in signals undetectable at the wavelengths and resolutions of SCIAMACHY and GOSAT.

4.2 Rotational-Raman scattering

We computed the filling-in of the 866 nm Ca II line due to rotational-Raman scattering (RRS) using the scalar Linearized Discrete Ordinate Radiative Transfer code (LIDORT-RRS) of Spurr et al. (2008). Figure 4 shows the filling-in as in Fig. 2 but from rotational-Raman scattering (RRS) only. Although the amount of atmospheric

AMTD
5, 163–210, 2012

scattering is relatively small at these wavelengths, the RRS filling-in is apparent owing to the large depth of this solar line as similarly shown by Joiner et al. (2011a) for the K I line at 770 nm. The spectral signature is very similar to that of line filling from a spectrally flat additive signal. The filling-in owing to RRS is about a factor of 6 less than that due to an additive signal of 0.2 mW m^{-2} nm^{-1} sr^{-1} at SCIAMACHY resolution. This factor increases somewhat at higher spectral resolutions.

Figure 5 shows that the RRS filling-in dependence on surface albedo is relatively flat for albedos $>\sim$0.3. There is a small but significant dependence on both surface pressure and solar zenith angle (SZA). Figure 6 shows the SZA dependence in more detail as well as the dependence on satellite view zenith angle (VZA) and surface pressure. The SZA dependence is relatively small for SZA $< 60^{\circ}$, but increases rapidly for greater angles. The VZA dependence is small for typical angles viewed by SCIAMACHY.

4.3 Vibrational-Raman scattering

Vibrational Raman scattering (VRS) is commonly neglected in UV and visible retrieval algorithms as it is small compared with rotational-Raman scattering (RRS) (Burrows et al., 1996). However, the fractional contribution of VRS is larger in the NIR owing to higher values of solar radiation at excitation wavelengths as compared with emission wavelengths. The VRS frequency shifts between excitation and emission are $\Delta\nu \simeq 2331$ and 1555 cm^{-1} for N_2 and O_2, respectively, assuming pure vibrational transitions of the molecules (Heise and Schrotter, 1995). We assessed the VRS contribution to the filling-in of the 866 nm Ca II Fraunhofer line using the single scattering approximation of the radiative transfer equation. Along with photons only scattered in the atmosphere, we also accounted for photons first reflected from the surface and then scattered in the atmosphere.

Absolute differential Raman cross sections of the vibrational line at 488 nm at 90° measured by different authors for N_2 vary from 3.3×10^{-31} to 5.6×10^{-31} cm^2 str-mol^{-1} (Fenner et al., 1973). Here, we use a value of 5.5×10^{-31} cm^2 str-mol^{-1} that is consistent with data from Heise and Schrotter (1995). The ratio of O_2 to N_2 cross sections at

AMTD
5, 163–210, 2012

488 nm is assumed to be 1.3 (Fenner et al., 1973). We adopt a general form of phase functions for both the unshifted Cabannes line and wavelength shifted VRS lines as suggested by Danichkin et al. (1982). For the central Cabannes line in air, the depolarization ratio for unpolarized light is assumed equal to 0.00734 (Chance and Spurr, 1997). For VRS lines, we use values recommended by Danichkin et al. (1982), i.e., 0.043 and 0.099 for N_2 and O_2, respectively.

Figure 7 shows the VRS filling-in of the 866nm Ca II Fraunhofer line as a function of surface albedo. The maximum value of about 0.45 % occurs for a non-reflecting surface. VRS filling-in rapidly decreases with increasing surface albedo. For typical values of surface albedo over land (>0.2), the filling-in only weakly depends on surface albedo and does not exceed 0.02 % for SZA < 60°. Therefore, we neglect VRS in the remainder of this study.

5 Retrieval methodology

5.1 Fitting windows

The use of solar Fraunhofer lines substantially simplifies a space-based retrieval of F_s as compared with the O_2-A band as described by Joiner et al. (2011a) and Frankenberg et al. (2011a); atmospheric correction is unnecessary as long as observations are made at wavelengths not affected by atmospheric absorption. Joiner et al. (2011a) used the potassium (K) I line near 770 nm to derive an additive signal using GOSAT's TANSO-FTS. This line falls between several weak O_2 lines and can be observed in relative isolation with GOSAT's high spectral resolution. Here, we use the same GOSAT fitting window as Joiner et al. (2011a) (769.90–770.25 nm). We have a second fitting window between 758.45 and 758.85 nm, similar to that used by Frankenberg et al. (2011b). We scale the results from the 758 nm window by 0.696 and add them those from the 770 nm window to increase the signal-to-noise ratio (SNR) of the combined additive signal.

AMTD
5, 163–210, 2012

Of the solar lines shown in Fig. 1 (656, 850, 854, 866 nm), only the 866 nm Ca II line is relatively free of contamination by atmospheric water vapor absorption. We attempted to retrieve additive signals using all of these lines including the Hα line near 656 nm in SCIAMACHY channel 4. We found that it was extremely difficult to disentangle the filling-in signal from water vapor absorption. Therefore, in the remainder of this work, we focus solely on deriving an additive signal using the 866 nm Ca II solar line from SCIAMACHY with the spectral band 863.5–868.5 nm.

5.2 General approach

We use a variation of the approach implemented by Joiner et al. (2011a) to jointly retrieve a reflectivity-related parameter K and an additive signal. We denote the additive signal henceforth as "$\overline{F}$" and make no assumptions regarding its source. We use the above-mentioned spectral fitting windows with the following simplified model for the observed Earth spectral radiance $\boldsymbol{I}(\lambda)$ that assumes negligible atmospheric absorption and scattering:

$$\boldsymbol{I}(\lambda) = K\boldsymbol{E}(\lambda)^* + \overline{F}, \quad (1)$$

(Joiner et al., 2011a) where $\boldsymbol{E}(\lambda)^*$ is a reference spectrum ideally containing no filling-in from the source of interest. We note that if the reference spectrum contains filling-in from other sources, the retrieved value will reflect a residual additive signal from sources not present in the reference.

As in Joiner et al. (2011a), we assume a constant wavelength dependence of $\overline{F}$ over our relatively small fitting windows. We fit both constant and linear in wavelength coefficients for K (i.e., $K = K_0 + K_1[\lambda - \lambda_0]$) for the larger SCIAMACHY fitting window, but only a constant for the smaller GOSAT windows. The spectral dependence of atmospheric, cloud, and aerosol scattering is essentially constant over the relatively small narrow fitting windows used, so the neglect of it will have an insignificant effect on the retrieval of $\overline{F}$. Similarly, calibration of the reference spectrum $E(\lambda)^*$ does not affect

AMTD
5, 163–210, 2012

the derived value of $\overline{F}$, since any offset between the reference and observed spectra is absorbed in the parameter K. An error in absolute calibration of $I(\lambda)$, however, will produce an error in $\overline{F}$.

Similar to the approach of Joiner et al. (2011a), we use a standard weighted least squares fitting procedure. All wavelengths are weighted equally except for a few wavelengths within the GOSAT fitting window that are not used because they are affected by O_2 absorption.

5.3 Use of reference spectra

The main difference between our approach and that of Joiner et al. (2011a) is that we use spectral radiance measurements made over the cloudy ocean as a reference rather than a measured or computed solar irradiance spectrum. No further corrections to observed spectra are made. Our retrieval approach is insensitive to errors in the instrument line shape function or reference solar spectra as these are not used.

The main criterion for reference spectra used to derive $\overline{F}$ from a terrestrial source is that the reference spectra should represent the spectral shape of a solar Fraunhofer line without filling-in from the terrestrial source. There are several advantages of using cloudy Earth radiance spectra as a reference to derive a terrestrial additive signal as opposed to solar irradiance spectra (measured or computed). Firstly, the use of Earth spectra minimizes the so-called undersampling problem and eliminates errors due to inaccuracy of the assumed instrument line shape function. The undersampling problem and a proposed correction method have been discussed at length by Chance et al. (2005). However, we found that the proposed correction method did not achieve the desired accuracy owing to uncertainties in the instrument line shape function. Because the wavelength shifts are very small between ocean reference spectra and the land spectra of interest, problems due to undersampling are essentially eliminated. Corrections used by Joiner et al. (2011a), that account for under-sampling when referencing to observed solar spectra slightly shifted in wavelength as compared with Earth spectra, are not necessary.

AMTD
5, 163–210, 2012

Secondly, referencing to ocean spectra with similar continuum radiance values allows us to significantly reduce the errors from stray light, dark current, zero-level offset, and other instrumental effects that can produce a false filling-in. These effects should be present in the ocean reference spectra at approximately the same level as in land spectra. Therefore, the effects should be accounted for when deriving a terrestrial additive signal using Eq. (1).

Finally, using ocean spectra at similar radiance levels and SZAs as a reference will implicitly account for some of the filling-in due to RRS. RRS depends upon surface albedo as well as the mean pressure of the scattering surface. Here, we are using cloudy ocean data at similar SZAs and continuum radiance values to land spectra. Studies of the so-called optical centroid pressure (approximately, the reflectance-weighted mean pressure) of clouds over ocean at moderate reflectivities typical of vegetated land show that the clouds occur mainly between about 775 and 875 hPa (Joiner et al., 2011b). Deep convective and frontal clouds that have lower optical centroid pressures typically occur only at higher Lambertian-equivalent reflectivities (>~0.6). Therefore, the main difference in RRS filling-in between the cloudy ocean and land spectra is due to the different effective surface pressures. As shown in Fig. 5, this difference is small, but not negligible for the expected pressure differences, sometimes leading to negative retrieved values of $\overline{F}$. We must bear this difference in mind when examining our results. For regions with surface pressures higher than about 900 hPa, there may be unaccounted for filling-in due to RRS. However, for high-altitude land regions (<775 hPa) the reference ocean spectra may overestimate RRS filling-in.

Frankenberg et al. (2011b) used a different approach to account for instrumental artifacts; they utilized measurements over Antarctica to develop a parameterization for the false fluorescence produced by the zero-level offset in GOSAT data. They showed generally increasing amounts of false fluorescence with radiance levels with some wiggles and a downturn at the highest radiances in the S polarization. We found similar features using cloudy ocean data. With our approach, we are able to cover the full range of observed radiance values and see a downturn in the false fluorescence or

AMTD
5, 163–210, 2012

filling-in at the highest radiance levels also in the P polarization. Our utilization of cloudy ocean data does not necessitate the use of high SZA data to cover the full range of observed continuum radiance values; filling-in from RRS increases rapidly at high SZAs as shown above, although the imprint of RRS is not obvious in the results of Frankenberg et al. (2011b).

Frankenberg et al. (2011b) discarded GOSAT P polarization data because the errors in that polarization were time-dependent. We likewise find such time-dependent errors in both GOSAT and SCIAMACHY data. Because cloudy ocean data are available year round, we are able to account for these errors and use all data including GOSAT P polarization, thereby significantly reducing the effects of instrumental noise.

In addition, cloudy ocean data span all latitudes. Therefore, we are able to account for instrumental effects that vary systematically with orbital phase; our approach is able to detect and correct for subtle but significant latitudinally-dependent artifacts in both GOSAT and SCIAMACHY data. We find that the latitudinal-dependence of these artifacts also varies with season.

Here, we binned potential reference spectra according to several criteria discussed below. For each bin, we averaged multiple spectra to produce a composite reference spectrum. To reduce any filling-in signal from the ocean, e.g., from ocean Raman scattering (Vasilkov et al., 2002) or fluorescence, we only use observations with reflectances > 0.2 for SCIAMACHY. For GOSAT we used only observations with a cloud fraction (derived from the CAI) of >20 %.

5.3.1 SCIAMACHY binning

For SCIAMACHY, we binned spectra separately for each of the two primary pixel exposure times and for each scan position within a nadir block according to the continuum radiance value and the wavelength shift (with respect to a fixed solar spectrum). We found that the observed filling-in over ocean sometimes changes abruptly and that it also drifts slowly over time. We therefore compute a set of reference spectra for each

AMTD
5, 163–210, 2012

day of observations. If the standard deviation of the filling-in over ocean for a given day is high, we eliminate that day from our sample.

We use a bin size of 0.1 for (normalized) radiance, represented by $R\cos(\mathrm{SZA})$ where R is the reflectance. We found that the wavelength shifts varied systematically with latitude, so binning by both wavelength shift and reflectivity implicitly accounts for filling-in features such as RRS that are function of solar zenith angle as well as instrumental artifacts that vary systematically with orbital phase. Because the wavelength shifts vary with time, we compute the daily mean and standard deviation of wavelength shift and use 8 bins with intervals of half the standard deviation of the wavelength shift (typically ~0.007 nm).

5.3.2 GOSAT binning and additional corrections

For GOSAT, we used bin sizes of 0.05 for normalized radiance, 20° for latitude, and 0.001 nm for wavelength shift. We use only data processed with the H gain range as there are not enough data from the M range to perform a reliable correction. Therefore, data over the Sahara and in parts of central Australia have not been processed. For GOSAT, we retrieve $\overline{F}$ separately for the S and P polarizations (separate corrections applied) and combine them. We also apply a correction factor to the radiances to account for instrument degradation as suggested by Kuze et al. (2011a).

5.4 Cloud filtering

Because clouds do not alter the spectral structure used to retrieve $\overline{F}$, we can tolerate small to moderate amounts of cloud within our satellite footprints; the main effect of clouds will be to shield a portion of the terrestrial additive signal from satellite view. We remove significantly cloud-contaminated data from our samples by two different methods. For SCIAMACHY, we use the concept of the cloud radiance fraction (CRF). CRF is defined as the fraction of observed radiance that is scattered by cloud particles. The CRF is a convenient quantity for cloud screening, because it can be computed directly for large fields-of-view and collocation with a subpixel imager is not necessary.

AMTD
5, 163–210, 2012

The CRF is given by

$$\mathrm{CRF} = f\frac{I_{\mathrm{cld}}}{I_{\mathrm{obs}}}, \tag{2}$$

where f is the geometric cloud fraction, and I_{obs} and I_{cld} are the observed and bare-cloud (no surface reflection) radiances, respectively. Here we use the so-called mixed Lambertian-Equivalent Reflectivity model to estimate the CRF. In this model, I_{cld} is specified as a Lambertian surface with an equivalent reflectivity of 0.8, and f is set equal to an effective cloud fraction f_{eff} that is derived using the relationship

$$I_{\mathrm{obs}} = f_{\mathrm{eff}} I_{\mathrm{cld}} + (1 - f_{\mathrm{eff}}) I_{\mathrm{clr}}. \tag{3}$$

(e.g., see Stammes et al., 2008, for an overview of the approach that has been used to retrieve the cloud optical centroid pressure at NIR through UV wavelengths). In short, the selection of 0.8 as the cloud reflectivity produces an effective cloud fraction that is generally less than the geometric cloud fraction and represents the fraction of the footprint that does not see the ground. Absorption and/or scattering from beneath a thin cloud is accounted for by the second term in Eq. (3).

Here, we neglect atmospheric scattering as it is very small at 866 nm. To compute I_{clr}, we use the black-sky 16-day gridded filled-land surface albedo product from Aqua MODIS (MOD43B3) at 865 nm (Lucht et al., 2000). We include only observations with CRF <10 % in our sample. Uncertainty in the SCIAMACHY absolute calibration relative to that of MODIS cause this check to allow a significant fraction of the data into our sample. Application of more or less stringent limits on cloud contamination within a moderate range did not substantially alter the derived spatial patterns of $\overline{F}$.

We calculated the fraction of a field-of-view for which the satellite does not sense the surface (f_{eff}) for various cloud conditions. We can express f_{eff} as a linear function of the geometrical cloud cover f_{g}, i.e., $f_{\mathrm{eff}} = A \times f_{\mathrm{g}}$, where A is a parameter that depends upon surface and cloud optical properties. For a surface albedo of 0.2, $A = \sim 0.5$ for a cloud optical thickness (τ) of 10 (using the C1 cloud model) and $A = 0.75$ for $\tau = 20$ at 760 nm

AMTD
5, 163–210, 2012

(results will be similar at 866 nm). Increasing surface albedo to 0.4 gives $A = \sim 0.4$ for $\tau = 10$ and $A = 0.75$ for $\tau = 20$. This implies that in partial cloud cover with typical values of τ (~ 10), a significant fraction of the surface is still seen by satellites. For example, in 40 % cloud cover with $\tau < 10$ and for surface albedos typical of vegetated land, 80 % or more of the surface signal is still seen.

Owing to uncertainty in the absolute calibration of GOSAT, here we use the geometrical cloud fraction derived from the GOSAT CAI. We removed observations with f_g >40 %. Derived spatial and temporal variations of additive signals did not depend substantially on the exact values of the thresholds used here for either GOSAT or SCIAMACHY.

5.5 Quality control

To create gridded data sets, we tested different filtering schemes for quality control. For SCIAMACHY, we included all data passing gross quality assurance checks on the filling-in, radiance residuals, and wavelength shifts. These checks remove very few observations. We also tested whether elimination of the initial scan positions within a nadir-viewing block of observations affected the monthly means. As this did not significantly affect the monthly means, all swath positions are included here. For GOSAT, we removed outliers ($> 2\sigma$) separately for P and S polarization data as well as for the combined P and S data.

5.6 Scaled fluorescence

When comparing the derived additive signals with vegetation indices, we use a quantity called "scaled-F" (Joiner et al., 2011a), defined as the retrieved $\overline{F}$ divided by cos(SZA). This scaling roughly accounts for variations in $\overline{F}$ due to the incoming (clear-sky) PAR.

5.7 Uncertainties

Uncertainties for GOSAT retrievals were calculated by Joiner et al. (2011a) assuming only random errors (i.e., instrumental noise). However, errors from unaccounted-for

AMTD
5, 163–210, 2012

systematic instrumental errors were quite significant. The absolute GOSAT $\overline{F}$ values in this work are smaller (by approximately a factor of 2) than those derived by Joiner et al. (2011a), owing to the new corrections applied.

Because unaccounted-for systematic errors in SCIAMACHY data could be significant and their magnitudes are unknown, it is difficult to quantify the uncertainties in the derived scaled-F. Many SCIAMACHY observations are available for averaging as compared with GOSAT which helps reduce random errors. However, systematic errors are expected to remain. For example, in addition to residual errors left over from imperfect corrections, the South Atlantic anomaly (SAA) has been known to affect measurements over South America. Here, we provide standard errors for gridbox averages to indicate uncertainty in the mean values. We note that there may still be significant errors in the derived absolute values of $\overline{F}$ and scaled-F. We also note that theoretical error calculations based on the assumption of random, Gaussian errors are likely to be invalid.

6 Results and discussion

6.1 Spatial variations in scaled-F

Figure 8 shows retrieved gridded monthly mean scaled-F for July and December 2009 derived from GOSAT at 770 nm and 758 nm (0.696*758 nm + 770 nm) and from SCIAMACHY at 866 nm. The values from SCIAMACHY at 866 nm are significantly smaller than those at 770 nm, as would be expected if the signals originate from chlorophyll-a fluorescence associated with the declining emission tail throughout the NIR region. Similar seasonal variation in scaled-F is seen by both sensors as well as EVI, namely, higher Northern Hemisphere values in July versus higher values in the Southern Hemisphere in December. Similar spatial patterns are shown in scaled-F by both SCIAMACHY and GOSAT, such as low values over central Brazil in July and over the northeast of Brazil in December. These variations in GOSAT and SCIAMACHY scaled-F are consistent with a vegetation source such as fluorescence. Like the EVI,

AMTD
5, 163–210, 2012

a retrieved fluorescence signal (scaled by incoming PAR) is sensitive to the amount of green biomass contained within the sensor field-of-view or fractional amount of intercepted PAR.

Subtle differences in spatial variations are shown between GOSAT- and SCIAMACHY–derived scaled-F. SCIAMACHY shows somewhat lower values at high northern latitudes in the boreal summer as compared with tropical regions. There could be several reasons for this if the primary source of the SCIAMACHY signal is vegetation fluorescence as is presumably the case for the GOSAT observations. Firstly, there may be remaining errors due to instrumental effects. Secondly, SCIAMACHY and GOSAT observations are made at different local times; SCIAMACHY observations are made near 10:00 LT while those of GOSAT are made about 2.5 h later, just after noon. The shapes of the fluorescence spectra may differ for different types of vegetation as well as different magnitudes and spectral shapes of the incoming solar light. For example, more UV light is absorbed in relatively clear skies at the surface in the tropics where total column ozone and SZAs are low. Plants at these latitudes have more photo-protective mechanisms in place that may produce different fluorescent spectral responses. Compounds within the vegetation besides chlorophyll-a may alter the spectral dependence of fluorescence. Finally, canopy structure may influence the fluorescence spectra. Multiple scattering within a deep canopy may enhance fluorescence, producing a different spectral response than a sparse canopy (Rosema et al., 1991).

Figures 9–10 show monthly climatologies of scaled-F and reflectance derived from over 8 yr of SCIAMACHY data (January 2003–September 2011, gridded at $0.5^{\circ} \times 0.5^{\circ}$ resolution) and EVI from Aqua MODIS (August 2002–July 2011 at the same spatial resolution) for comparison. An animated version of the SCIAMACHY scaled-F climatology is available in the supplemental material. The general spatial and temporal patterns from SCIAMACHY scaled-F are similar to EVI and consistent with fluorescence related to vegetation. Note that we show scaled-F here for solar zenith angles up to 80°. In the winter hemisphere at the highest latitudes shown, scaled-F originating from a

AMTD
5, 163–210, 2012

terrestrial source is likely to be overestimated owing to atmospheric RRS that is not fully accounted for.

Some interesting differences between scaled-F and EVI are shown here as well as in Fig. 8. For example, we see moderate values of EVI over parts of the northeast and southeast US, Europe, and southeast Asia in the late autumn through early spring while scaled-F is close to zero. The values of scaled-F are more distinctly lower over parts of east and northeast Brazil from May through November as compared with the EVI. These differences are further explored in the next subsection.

Scaled-F is shown to be loosely correlated with reflectance in vegetated areas. This would be expected if the additive signal at the Ca II line has a vegetation source. However, there are also areas of high reflectance with low $\overline{F}$ such as over the Sahara and parts of the Saudi Arabian peninsula. This demonstrates that the additive signal is not entirely related to reflectivity as might be the case if the signal was entirely due to instrumental artifacts. This is also consistent with a vegetation source for the 866 nm additive signals.

6.2 Seasonal variations in SCIAMACHY and GOSAT scaled-F and EVI

In Fig. 12, we examine the climatological seasonal cycle of scaled-F from both SCIAMACHY and GOSAT (reduced by a constant factor of 6) as well as EVI over several geographic regions shown in Fig. 11. We show examples for several different biome types, using the same scales in all panels to highlight differences between scaled-F and EVI for the different regions and vegetation types.

Over the deciduous broadleaf forests of the northeast US (Fig. 12, panel 1), SCIAMACHY scaled-F shows seasonal variations similar to those of GOSAT. GOSAT has larger uncertainties owing to smaller numbers of observations. Like scaled-F, the EVI shows a sharp rise starting around May and a decline starting in September. For evergreen needleleaf (pine) forests in the southeast US (panel 2), seasonal variations are similar for SCIAMACHY scaled-F and EVI. GOSAT scaled-F also shows a rise in April and decline starting in September. For these and many other moderate to high latitude

AMTD
5, 163–210, 2012

regions, values of the EVI have minima between 0.2 and 0.5 during winter months, while scaled-F is near zero.

In the heavily forested areas of the central Amazon (panel 3), both the EVI and scaled-F remain relatively high year round. This contrasts sharply with shrubland over northeast Brazil (panel 4) at similar latitudes. Here, scaled-F and EVI are low in August through November following the wet season green-up when scaled-F and EVI both peak in April.

The savannas of central Africa (panel 5) have a distinct and similar seasonal cycle in scaled-F and EVI. Scaled-F from SCIAMACHY shows an earlier peak than that of GOSAT over croplands of India (panel 6). GOSAT scaled-F also peaks earlier than EVI.

Although we have shown some differences between EVI and scaled-F, the similarity of the SCIAMACHY and GOSAT scaled-F temporal and spatial variations and the comparisons with EVI appear to be consistent with a major source of the scaled-F signals linked to vegetation. A plausible explanation is that fluorescence from chlorophyll-a contributes to scaled-F at wavelengths near the O_2-A band as well as at 866 nm. The spatial and temporal patterns are not consistent with fire as a dominant source, though we note that fires may contribute to the observed signals.

6.3 Filling-in not consistent with vegetation fluorescence

We note a significant filling-in (retrieved as $\overline{F}$) at 866 nm over parts of the Sahara desert (most apparent in May–September) and the Saudi Arabian peninsula where vegetation is sparse and a significant signal from chlorophyll fluorescence is not expected. These signals sometimes, but not always, occur over very high albedo surfaces. Examination of residual filling-in over Greenland (not shown) indicates residual filling-in over only the brightest areas that may not have been well characterized by the cloudy ocean spectra. Cloudy spectra with high radiance values occur primarily in deep and frontal convection where cloud pressures are low. This may lead to an underestimation of filling-in from RRS when these spectra are used as a reference and thus over-estimation of the residual filling-in from terrestrial sources.

AMTD
5, 163–210, 2012

Filling-in over barren regions may also be produced by luminescent minerals in soil and/or rock. There are many types of minerals with impurities that luminesce when excited by UV and visible light (Gaft et al., 2005). For example, samples of fluorite (CaF_2) containing Nd^{3+} (Neodymium) centers show laser-induced luminescence with peaks at 866 and 795 nm (Gaft et al., 2005). Similarly, Dy^{3+} (Dysprosium) centers give narrow peaks at 765 and 778 nm.

High scaled-F values are also frequently seen around continental and island coastlines, particularly on the Eastern edges. No such features are present in the reflectance climatology shown in Figs. 9–10. These high values may be due to an oceanic source of additive signal, a spatial aliasing effect, or some other instrumental artifact such as distortion of the spectral response function (SRF) in the presence of large radiance gradients within a satellite footprint. We observed neither high radiance residuals nor large wavelength shifts that may accompany errors due to distortion of the SRF.

7 Conclusions and ongoing work

Our simulations indicate that terrestrial fluorescence filling-in of the 866 nm Ca II line can be detected using hyperspectral instruments (spectral resolutions of the order of tenths of a nm) such as SCIAMACHY if the fluorescence at this wavelength is of the order of 0.1–0.2 $mW\,m^{-2}\,nm^{-1}\,sr^{-1}$. After corrections for instrumental artifacts, we retrieved an additive signal over land at 866 nm with SCIAMACHY. The magnitude of the derived additive signal at 866 nm is similar to that of our solar-simulator laboratory measurements. The spatial and temporal patterns of the detected additive signals at 866 nm are consistent with a vegetation source; they are similar to those of EVI and those derived from additive signals at 770 and 758 nm where fluorescence from chlorophyll-a in vegetation is stronger and expected to be the primary source of the signals. Further laboratory and ground-based studies are needed to confirm that the additive signal retrieved at 866 nm is indeed primarily due to vegetation fluorescence. Measurements of fluorescence and reflectance spectra for a variety of vegetation types,

AMTD
5, 163–210, 2012

canopy structures, illumination, and environmental conditions will help to improve the interpretation of satellite-derived additive signals shown here. Additional sources of the additive signals include unaccounted-for vibrational and rotational-Raman scattering in the atmosphere, fluorescence from minerals in rock and soil, flaming fires, and volcanoes.

Owing to the large number of observations collected over more than 8 yr of operation, SCIAMACHY data can be averaged to provide climatological spatial patterns of $\overline{F}$ at a higher resolution than is possible with the current set of GOSAT observations, even though the intrinsic spatial resolution of SCIAMACHY is lower than that of GOSAT. Although the derived spatial patterns and seasonal cycles in scaled-F are similar to those of the MODIS EVI, important differences between scaled-F and EVI are noted. For example, a more distinct shut-off of activity in winter and dry months is shown in scaled-F in some areas as compared with EVI, which could improve estimates of the length of the physiologically-active growing season.

More work needs to be done to further refine $\overline{F}$ retrievals from satellite instruments that were not designed to measure small additive signals. Owing to the extremely small $\overline{F}$ signal derived from instruments that have relatively large systematic errors, our reported absolute values and temporal/spatial variations may still contain residual errors. However, the approach we developed appears to be capable of detecting and correcting for complex, time-varying instrumental artifacts.

In addition, more research is needed to fully exploit these data within global carbon models and other applications. For example, the influences of canopy structure and other large-scale parameters, such as chlorophyll content, need to be further investigated in order to understand their effect on large field-of-view satellite data (e.g., Rosema et al., 1991; Louis et al., 2005; Meroni and Colombo, 2006; Middleton et al., 2008; van der Tol et al., 2009; Zarco-Tejada et al., 2009; Rascher et al., 2009; Damm et al., 2010). It has been suggested that when vegetation is not under stress and the variations in fluorescence yield are small, fluorescence flux from the 740 nm emission feature, that is not affected by reabsorption, contains direct information about absorbed

AMTD
5, 163–210, 2012

PAR (Moya et al., 2004). In addition, the ratio of fluorescence from the 740 and 680 nm features expresses information about chlorophyll concentration (e.g., Gitelson et al., 1999; Saito et al., 1998; Louis et al., 2005). Therefore, additional measurements of fluorescence at other wavelengths will be useful for disentangling the yield information from the chlorophyll content. In order to more fully exploit satellite-derived fluorescence measurements for deriving relationships with key carbon-related parameters such as gross primary production (GPP) or light-use efficiency (LUE), they should be combined with other observable quantities such as the reflectance-based vegetation indices including the PRI (Daumard et al., 2010).

The upcoming launch of the Orbiting Carbon Observatory-2 (OCO-2) (Crisp et al., 2004) will facilitate the use of solar Fraunhofer lines for fluorescence retrievals at wavelengths near the O_2-A band (Frankenberg et al., 2011a) and provide more opportunities for fluorescence measurements. The FLuorescence EXplorer (FLEX) (Rascher, 2007; European Space Agency, 2008), an ESA Explorer Mission selected for Phase A/B1 in early 2011, plans to utilize the O_2-A and B bands for chlorophyll fluorescence retrievals (Guanter et al., 2010). FLEX would provide fluorescence information at a higher spatial resolution than current satellite sensors that were not designed or optimized for fluorescence retrievals.

Appendix A

Instrumental effects in SCIAMACHY data that may produce false filling-in

A1 Memory effect

In channels 1–5, it was found that the signal deviates from a linear response. The deviation depends upon the signal level of the previous readout. It also depends on the signal level including analog offset and dark current. Since there is a dependence on the previous signal for a large range of detector fillings, artificial spectral features can be introduced into the measurements.

AMTD
5, 163–210, 2012

We found systematic biases in Fraunhofer line filling as a function of position within a block of nadir measurements. The first several positions (following the limb-viewing mode) have the largest biases. Because of repeating orbital patterns, if this effect is not accounted for, a cross-track striping will be present in the observed filling-in, even after averaging a month of data.

A2 Dark current

There are two components that contribute to the dark signal in channels 1–5: the analog offset and the leakage current. The former does not depend on integration time while the latter does. We found different biases in the filling-in for the two primary pixel exposure times (PETs) used for nadir measurements in channels 4 and 5 that may be a result of unaccounted for dark signals.

A3 Wavelength calibration and undersampling

Due to the Doppler and other effects, there are small wavelength shifts in Earth spectra with respect to the measured solar spectra. We found that these wavelength shifts vary systematically with latitude. Wavelength shifts between observed and reference spectra must be accurately accounted for when deriving a relatively small filling-in signal.

A4 Straylight

Stray light may be classified as two types: spectral and spatial. Both of these can distort observed spectra. Spatial stray light mainly affects the limb measurements of SCIAMACHY, but may also produce errors in a fluorescence retrieval in the nadir mode. Spectral stray light may be caused by diffuse reflection that adds signal to all detector pixels in a given channel, thus mimicking fluorescence. The largest expected uniform stray light fraction in SCIAMACHY is 0.14 % (Lichtenberg et al., 2006).

AMTD
5, 163–210, 2012

So-called “ghost” stray light is caused by reflection from one wavelength to another. It does not add signal to all pixels equally, but can distort the spectrum. The correction method is accurate to around 25 %, leaving at most 1 % stray light in the spectrum.

A5 Calibration

Various issues with SCIAMACHY’s radiometric calibration are discussed by Lichtenberg et al. (2006). These may affect the absolute values of derived fluorescence. In addition to radiometry, the applied calibration scheme may introduce spectral features and thus produce false filling-in.

Supplementary material related to this article is available online at: http://www.atmos-meas-tech-discuss.net/5/163/2012/amtd-5-163-2012-supplement.zip.

Acknowledgements. Funding for this work was provided by the NASA Carbon Cycle Science program (NNH10DA001N) managed by Diane E. Wickland and Richard Eckman. The authors are indebted to C. Retschler for assistance with the satellite data sets, particularly the SCIAMACHY data. We gratefully acknowledge the European Space Agency, the GOSAT project, and the MODIS data processing team for making available the SCIAMACHY, GOSAT, and MODIS data, respectively, used here. We also thank W. Philpot, W. Cook, K. F. Huemmrich, Y.-B. Cheng, Q. Zhang, J. Mao, C. Weaver, D. Crisp, and A. da Silva for helpful discussions.

References

Amoros-Lopez, J., Gomez-Chova, L., Vila-Frances, J., Alonso, L., Calpe, J., Moreno, J., and del Valle-Tascon, S.: Evaluation of remote sensing of vegetation fluorescence by the analysis of diurnal cycles, Int. J. Remote Sens., 29, 5423–5436, 2008. 167, 169

AMTD
5, 163–210, 2012

Burrows J., Vountas, M., Hang, H., Chance, K., Marquard, L., Muirhead, K., Platt, U., Richter, A., and Rozanov, V.: Study of the Ring effect, ESA final report, 1996. 174
Campbell, P. K. E., Middleton, E. M., Corp, L. A., and Kim, M. S.: Contribution of chlorophyll fluorescence to the apparent vegetation reflectance, Sci. Total Environ., 404, 433–439, 2008. 166, 169
Chance, K. V. and Spurr, R. J. D.: Ring effect studies: Rayleigh scattering, including molecular parameters for rotational Raman scattering, and the Fraunhofer spectrum, Appl. Opt., 36, 5224–5230, 1997. 175
Chance, K. and Kurucz, R. L.: An improved high-resolution solar reference spectrum for Earth's atmosphere measurements in the ultraviolet, visible, and near infrared, J. Quant. Spectrosc. Radiat. Trans., 111, 1289–1295, 2010. 172
Chance, K., Kurosu, T. P., and Sioris, C. E.: Undersampling correction for array detector-based satellite spectrometers, Appl. Opt., 44, 1296–1304, 2005. 177
Chappelle, E. W. and Williams, D. L., Laser-induced fluorescence (LIF) from plant foliage, IEEE T. Geosci. Remote , GE-25, 726–736, 1987. 169, 170
Chappelle, E. W., Wood, F. M., McMurtrey, J. E., and Newcomb, W. W.: Laser-induced fluorescence of green plants. 1: A technique for the remote detection of plant stress and species differentiation, Appl. Opt., 23, 134–138, 1984. 169
Corp, L. A., McMurtrey, J. E., Middleton, E. M., Mulchi, C. L., Chappelle, E. W., and Daughtry, C. S. T.: Fluorescence Sensing Systems: In vivo detection of biophysical variations in field corn due to nitrogen supply, Remote Sens. Environ., 86, 470–479, 2003. 166
Corp, L. A., Middleton, E. M., McMurtrey, J. E., Campbell, P. K. E., and Butcher, L. M.: Fluorescence sensing techniques for vegetation assessment, Appl. Opt., 45, 1023–1033, 2006. 166
Crisp, D.: The Orbiting Carbon Observatory (OCO) mission, Adv. Space Res., 34, 700–709, 2004. 189
Damm, A., Elbers, J., Erler, A., Giolis, B., Hamdi, K., Hutjes, R.W.A., Kosvancova, M., Meroni, M., Miglietta, F., Moersch, A., Moreno, J., Schickling, A., Sonnenschein, R., Udelhoven, T., Linden, S., Van Der, Hostert, P., and Rascher, U.: Remote sensing of sun-induced fluorescence to improve modeling of diurnal courses of gross primary production (GPP), Glob. Change Biol., 16, 171–186, doi:10.1111/j.1365-2486.2009.01908.x, 2010. 166, 188
Danichkin, S. A., Eliseev, A .A., Popova, T. N., Ravodina, O. V., and Stenina, V. V.: Raman scattering parameters for gas molecules (Review), J. Appl. Spectrosc., 35, 1057–1066, 1982.

AMTD
5, 163–210, 2012

175
Deutsches Zentrum fur Luft- und Raumfahrt: SCIAMACHY Level 1b-1c processing The SciaL1c Command-line tool software user's manual, ENV-SUM-DLR-SCIA-0071, Issue 6.0, 2006. 170
Daumard, F., Champagne, S., Fournier, A., Goulas, Y., Ounis, A., Hanocq, J.-F., and Moya, I.: A field platform for continuous measurement of canopy fluorescence, IEEE T. Geosci. Remote., 48, 3358–3368, 2010. 167, 189
Edner, H., Johansson, J., Svanberg, S., and Wallinder, E.: Fluorescence lidar multicolor imaging of vegetation, Appl. Opt., 33, 2471–2479, 1994. 169
European Space Agency:. ESA SP-1313/4 Candidate Earth Explorer Core Missions – Reports for Assessment: FLEX – FLuorescence EXplorer, published by ESA Communication Production Office, Noordwijk, The Netherlands, available at: http://esamultimedia.esa.int/docs/SP1313-4_FLEX.pdf., 2008. 189
Fenner W. R., Hyatt, H. A., Kellam, J. M. and Porto, S. P. S.: Raman cross section of some simple gases, J. Opt. Soc. America, 63, 73–77, 1973. 174, 175
Flexas, J., Escalona, J. M., Evain, S., J. Gulías, Moya, I., Osmond, C. B., and Medrano, H.: Steady-state chlorophyll fluorescence (Fs) measurements as a tool to follow variations of net CO_2 assimilation and stomatal conductance during water-stress in C_3 plants, Physiologia Plantarum, 114, 231–240, 2002. 166
Frankenberg, C., Butz, A., and Toon, G. C.: Disentangling chlorophyll fluorescence from atmospheric scattering effects in O2A-band spectra of reflected sun-light, Geophys. Res. Lett., 38, L03801, doi:10.1029/2010GL045896, 2011a. 166, 167, 175, 189
Frankenberg, C., Fisher, J. B., Worden, J., Badgley, G., Saatchi, S. S., Lee, J.-E., Toon, G. C., Butz, A., Jung, M., Kuze, A., and Yokota, T.: New global observations of the terrestrial carbon cycle from GOSAT: Patterns of plant fluorescence with gross primary productivity, Geophys. Res. Lett., 38, L17706, doi:10.1029/2011GL048738, 2011b. 166, 167, 171, 175, 178, 179
Gaft, M., Reisfeld, R., and Panczer, G.: Modern luminescence spectroscopy of minerals and materials, Spring-Verlag, Berlin, Heidelberg, 356 pp., 2005. 187
Gitelson, A. A., Buschmann, C., and Lichtenthaler, H. K.: The chlorophyll fluorescence ratio F_{735}/F_{700} as an accurate measure of chlorophyll content in plants, Remote Sens. Environ., 69, 296–302, 1999. 189
Gottwald, M., Bovensmann, H., Lichtenberg, G., Noel, S., von Bargen, A., Slijkhuis, S., Piters, A., Hoogeveen, R., von Savigny, C., Buchwitz, M., Kokhanovsky, A., Richter, A., Rozanov,

AMTD
5, 163–210, 2012

A., Holzer-Popp, T., Bramstedt, K., Lambert, J.-C., Skupin, J., Wittrock, F., Schrijver, H., and Burrows, J. P.: SCIAMACHY, Monitoring the Changing Earth's Atmosphere, Published by DLR and Springer, doi:10.1007/978-90-481-9896-2, 2006. 170

Guanter, L., Alonso, L., Gómez-Chova, L., Amorós-López, J., Vila-Francés, J., and Moreno, J.: Estimation of solar-induced vegetation fluorescence from space measurements, Geophys. Res. Lett., L08401, doi:10.1029/2007GL029289, 2007. 167

Guanter, L., Alonso, L., Gómez-Chova, Meroni, M., Preusker, R., Fischer, J., and Moreno, J.: Developments for vegetation fluorescence retrieval from spaceborne high-resolution spectrometry in the O_2-A and O_2-B absorption bands, J. Geophys. Res., 115, D19303, doi:10.1029/2009JD013716, 2010. 189

Heise, H. M. and Schrotter, H. W.: Rotation-vibration spectra of gases, Infrared and raman Spectroscopy, Methods and Applications, VCH, Weinheim, Chapt. 4.3, 253–297, 1995. 174

Hemphill, W. R., and Vickers, R.: Geological studies of the Earth and planetary surfaces of ultraviolet absorption and stimulated luminescence, NASA Tech. Lett. NASA-33, Washington, DC, USA, 1966. 168

Hemphill, W. R., Tyson, R. M., and Theisen, A. F.: Spectral luminescence properties of natural specimens in the scheelite-powellite series, and an assessment of their detectivity with an airborne Fraunhofer line discriminator, Econ. Geol., 83, 637–646, 1988. 168

Huete, A. R., Didan, K., Miura, T., Rodriguez, E. P., Gao, X., and Ferreira, L. G.: Overview of the radiometric and biophysical performance of the MODIS vegetation indices, Remote Sens. Environ., 83, 195–213, 2002. 172

Joiner, J., Yoshida, Y., Vasilkov, A. P., Yoshida, Y., Corp, L. A., and Middleton, E. M.: First observations of global and seasonal terrestrial chlorophyll fluorescence from space, Biogeosci., 8, 637–651, doi:10.5194/bg-8-637-2011, 2011a. 167, 171, 174, 175, 176, 177, 182, 183

Joiner, J., Vasilkov, A. P., Gupta, P., Bhartia, P. K., Veefkind, P., Sneep, M., de Haan, J., Polonsky, I., and Spurr, R.: Fast simulators for satellite cloud optical centroid pressure retrievals, 1. evaluation of OMI cloud retrievals, Atmos. Meas. Tech. Discuss., 4, 6185–6228, doi:10.5194/amtd-4-6185-2011, 2011b. 178

Kuze, A., Suto, H., Nakajima, M., and Hamazaki, T.: Thermal and near infrared sensor for carbon observation Fourier-transform spectrometer on the Greenhouse Gases Observing Satellite for greenhouse gases monitoring, Appl. Opt., 48, 6716–6733, 2009. 171

Kuze, A., O'Brien, D. M., Taylor, T. E. , Day, J. O, O'Dell, C., Kataoka, F., Yoshida, M., Mitomi, Y., Bruegge, C., Pollock, H., Basilio, R., Helmlinger, M., Matsunaga, T., S.

AMTD
5, 163–210, 2012

Kawakami, S., Shiomi, K., Urabe, T., and Suto H.: Vicarious calibration of the GOSAT sensors using the Railroad Valley desert playa, IEEE T. Geosci. Remote, 49, 1781–1795, doi:10.1109/TGRS.2010.2089527, 2011a. 171, 180

Kuze, A., Suto, H., Shiomi, K., and Nakajima, M.: GOSAT TANSO calibration and characterization of 2 years on orbit operation, Transaction of the Japan Society for Aeronautical and Space Science, Space Technology Japan, submitted, 2011b. 171

Lichtenberg, G., Kleipool, Q., Krijger, J. M., van Soest, G., van Hees, R., Tilstra, L. G., Acarreta, J. R., Aben, I., Ahlers, B., Bovensmann, H., Chance, K., Gloudemans, A. M. S., Hoogeveen, R. W. M., Jongma, R. T. N., Nol, S., Piters, A., Schrijver, H., Schrijvers, C., Sioris, C. E., Skupin, J., Slijkhuis, S., Stammes, P., and Wuttke, M.: SCIAMACHY Level 1 data: calibration concept and in-flight calibration, Atmos. Chem. Phys., 6, 5347–5367, doi:10.5194/acp-6-5347-2006, 2006. 170, 171, 190, 191

Louis, J., Ounis, A., Ducruet, J.-M., Evain, S., Laurila, T., Thum, T., Aurela, M., Wingsle, G., Alonso, L., Pedros, R., and Moya, I.: Remote sensing of sunlight-induced chlorophyll fluorescence and reflectance of Scots pine in the boreal forest during spring recovery, Remote Sens. Environ., 96, 37–48, 2005. 166, 188, 189

Lucht, W., Schaaf, C. B., and Strahler, A. H.: An Algorithm for the retrieval of albedo from space using semiempirical BRDF models, IEEE T. Geosci. Remote, 38, 977–998, 2000. 181

McFarlane, J. C., Watson, R. D., Theisen, A. F., Jackson, R. D., Ehrler, W. L., Pinter, P. J., Idso, S. B., and Reginato, R. J.: Plant stress detection by remote measurement of fluorescence, Appl. Opt., 19, 3287–3289, 1980. 167

Meroni, M. and Colombo, R.: Leaf level detection of solar induced chlorophyll fluorescence by means of a subnanometer resolution spectroradiometer, Remote Sens. Environ., 103, 438–448, 2006. 167, 188

Meroni, M., Picchi, V., Rossini, M., Cogliati, S., Panigada, C., Nali, C., Lorenzini, G., and Colombo, R.: Leaf level early assessment of ozone injuries by passive fluorescence and photochemical reflectance index, Int. J. Remote Sens., 29, 5409–5422, 2008. 166, 167

Meroni, M., Rossini, M., Guanter, L., Alonso, L., Rascher, U., Colombo, R., and Moreno, J.: Remote sensing of solar-induced chlorophyll fluorescence: Review of methods and applications, Remote Sens. Environ., 113, 2037–2051, 2009. 166, 167

Middleton, E. M., Corp, L. A., and Campbell, P. K. E.: Comparison of measurements and FluorMOD simulations for solar induced chlorophyll fluorescence and reflectance of a corn crop under nitrogen treatments, Intl. J. Rem. Sensing, Special Issue for the Second Inter-

AMTD
5, 163–210, 2012

national Symposium on Recent Advances in Quantitative Remote Sensing (RAQRSII), 29, 5193–5213, 2008. 167, 170, 188

Middleton, E. M., Cheng, Y.-B., Corp, L. A., Huemmrich, K. F., Campbell, P. K. E., Zhang, Q.-Y., Kustas, W. P., and Russ, A. L.: Diurnal and seasonal dynamics of canopy-level solar-induced chlorophyll fluorescence and spectral reflectance indices in a cornfield, Proc. 6th EARSeL SIG Workshop on Imaging Spectroscopy, CD-Rom, 12 pp., Tel-Aviv, Israel, 16–19 March, 2009. 167

Moya I., Camenen, L. Evain, S., Goulas, Y., Cerovic, Z.G., Latouche, G., Flexas, J., and Ounis, A.: A new instrument for passive remote sensing : 1. Measurements of sunlight-induced chlorophyll fluorescence. Remote Sens. Environ., 91, 186–197, 2004. 189

Plascyk, J. A. and Gabriel, F. C.: The Fraunhofer Line Discriminator MKII – An airborne instrument for precise and standardized ecological luminescence measurement, IEEE Trans. Instrum. Meas., 24, 306–313, 1975. 167

Rascher, U.: FLEX – Fluorescence Explorer: A remote sensing approach to quatify spatio-temporal variations of photosynthetic efficiency from space, Photosynth. Res., 91, 293–294, 2007. 189

Rascher, U., Agati, G., Alonso, L., Cecchi, G., Champagne, S., Colombo, R., Damm, A., Daumard, F., de Miguel, E., Fernandez, G., Franch, B., Franke, J., Gerbig, C., Gioli, B., Gómez, J. A., Goulas, Y., Guanter, L., Gutiérrez-de-la-Cámara, Ó., Hamdi, K., Hostert, P., Jiménez, M., Kosvancova, M., Lognoli, D., Meroni, M., Miglietta, F., Moersch, A., Moreno, J., Moya, I., Neininger, B., Okujeni, A., Ounis, A., Palombi, L., Raimondi, V., Schickling, A., Sobrino, J. A., Stellmes, M., Toci, G., Toscano, P., Udelhoven, T., van der Linden, S., and Zaldei, A.: CEFLES2: the remote sensing component to quantify photosynthetic efficiency from the leaf to the region by measuring sun-induced fluorescence in the oxygen absorption bands, Biogeosciences, 6, 1181–1198, doi:10.5194/bg-6-1181-2009, 2009. 167, 188

Rosema, A., Verhoef, W., Schoote, J., and Snel, J. F. H.: Simulating fluorescence light-canopy interaction in support of laser-induced fluorescence measurements, Remote Sens. Env., 37, 117–130, 1991. 169, 170, 184, 188

Saito, Y., Kanoh, M., Hatake, K., Kawahara, T. D., and Nomura, A.: Investigation of laser-induced fluorescence of several natural leaves for application to lidar vegetation monitoring, Appl. Opt., 37, 431–437, 1998. 169, 189

Sioris, C., Courrèges-Lacoste, G. B., and Stoll M. P.: Filling in of Fraunhofer lines by plant fluorescence: Simulations for a nadir-viewing satellite-borne instrument, Geophys. Res.

AMTD
5, 163–210, 2012

Lett., 108, 4133, doi:10.1029/2001JD001321, 2003. 167
Spurr, R. J. D., de Haan, J., van Oss, R., and Vasilkov, A. P.: Discrete ordinate radiative transfer in a stratified medium with first order rotational Raman scattering, J. Quant. Spectrosc. Ra., 109, 404–425, 2008. 173
Stacy, J. E., Breckinridge, J. B., Conel, J. E., and Chrisp, M. P.: Orbital Fraunhofer line discriminator feasibility study, Jet Propulsion Laboratory report D-1512, NASA FOIA Request No. 10-JPL-F-01288, 1984. 168
Stammes, P., Sneep, M., de Haan, J. F., Veefkind, J. P., Wang, P., and Levelt, P. F.: Effective cloud fractions from the Ozone Monitoring Instrument: Theoretical framework and validation, J. Geophys. Res., 113, D16S38, doi:10.1029/2007JD008820, 2008. 181
Thuillier, G., Hersé, M., Labs, D., Foujols, T., Peetermans, W., Gillotay, D., Simon, P. C., and Mandel, H.: The solar spectral irradiance from 200 to 2400 nm as measured by the SOLSPEC spectrometer from the ATLAS and EURECA missions, Solar Phys., 214, 1–22, 2003. 199
Thuillier, G., Floyd, L., Woods, T. N., Cebula, R., Hilsenrath, E., Hersé, M., and Labs D.: Solar irradiance reference spectra, in: Solar Variability and its Effect on the Earth's Atmosphere and Climate System, Geophysical Monograph, edited by: Pap, J., Fox, P., Frohlich, C., Hudson, H. S., Kuhn, J., McCormack, J., North, G., Sprigg, W., and Wu, S. T., Vol. 141, American Geophysical Union, Washington, DC, 171–194, 2004. 199
van der Tol, C., Verhoef, W., and Rosema, A.: A model for chlorophyll fluorescence and photosynthesis at leaf scale, Agricult. Forest Meteorol., 149, 96–105, 2009. 166, 188
Vasilkov, A. P., Joiner, J., Gleason, J. F., and Bhartia, P. K.: Ocean Raman scattering in satellite backscatter ultraviolet measurements, Geophys. Res. Lett., 29, 1837–1840, 2002. 179
Watson, R. D.: Airborne Fraunhofer line discriminator surveys in southern California, Nevada, and central New Mexico, Workshop of applications of luminescence techniques to Earth resource studies. A Lunar and Planetary Institute Workshop 10-12 December, 1980, in Houston, TX, USA, edited by: Hemphill, W. R. and Settle, M., Tech Rep. 81–03, LPI, Houston, TX., 28–35, 1981. 167, 168
Xu, L., Samanta, A., Costa, M. H., Ganguly, S., Nemani, R. R., and Myneni, R. B.: Widespread decline in greenness of Amazonian vegetation due to the 2010 drought, Geophys. Res. Lett., 38, L07402, doi:10.1029/2011GL046824, 2011. 172
Yokota, T., Yoshida, Y., Eguchi, N., Ota, Y., Tanaka, T., Watanabe, H., and Maksyutov, S.: Global Concentrations of CO_2 and CH_4 Retrieved from GOSAT: First Preliminary Results,

AMTD
5, 163–210, 2012

Sci. Online Lett. Atm., 5, 160–163, 2009. 171
Zarco-Tejada, P. J., Berni, J. A. J., Suarez, L., Sepulcre-Cantó, G., Morales, F., and Miller, J. R.: Imaging chlorophyll fluorescence with an airborne narrow-band multispectral camera for vegetation stress detection, Remote Sens. Environ., 113, 1262–1275, 2009. 167, 188

AMTD
5, 163–210, 2012

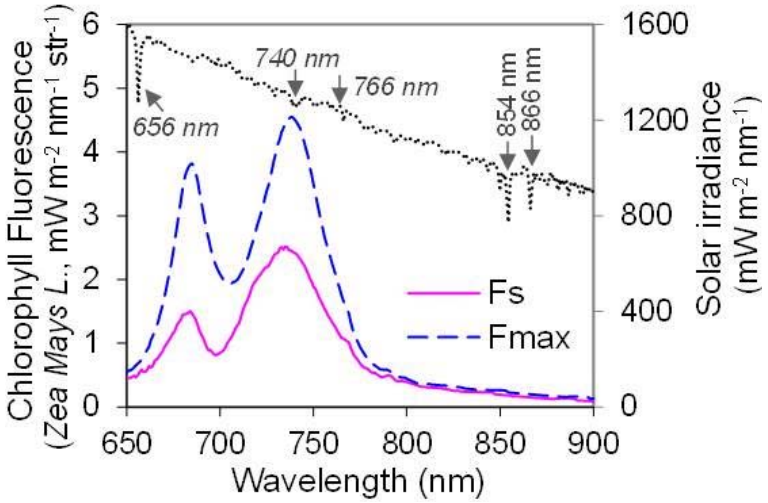

Fig. 1. Measured fluorescence spectra of excised corn leaves (Zea Mays L.) in the laboratory, with simulated solar illumination at full mid-day sun intensity as measured below a long-pass filter blocking wavelengths longer than 665 nm, showing maximum fluorescence (F_{max}) after 5 min. of dark adaptation, steady state fluorescence (F_s, achieved in less than 0.5 min after illumination), and a sample solar spectrum from Thuillier et al. (2003, 2004).

AMTD
5, 163–210, 2012

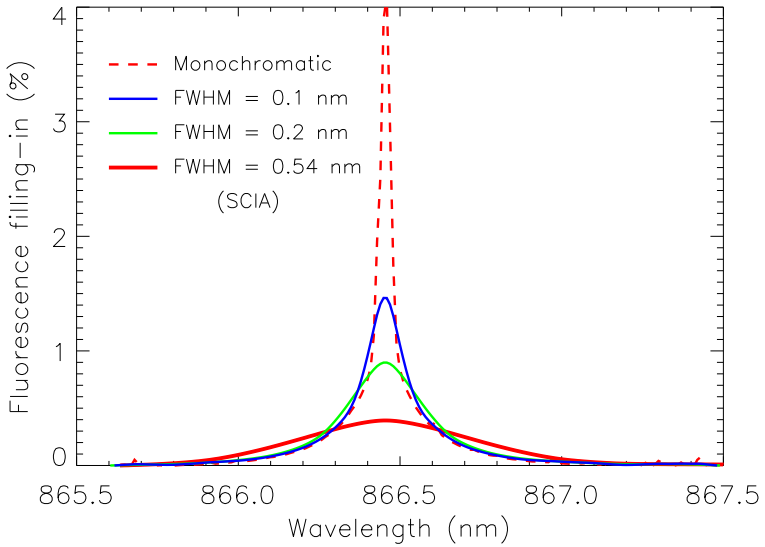

Fig. 2. Simulated spectral filling-in around the Ca II solar line from an additive signal of $0.2\,\mathrm{mW\,m^{-2}\,nm^{-1}\,sr^{-1}}$, SZA = 40°, nadir, and surface albedo = 0.3 (RRS not included) for different instrument resolutions (triangular slit function) with full-width half-maximum (FWHM) as indicated including that of SCIAMACHY (SCIA).

AMTD
5, 163–210, 2012

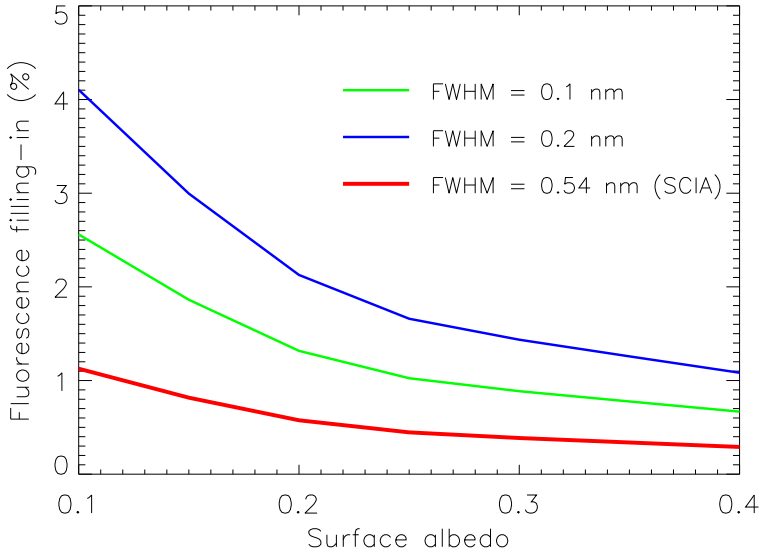

Fig. 3. Filling-in due to an additive signal of 0.2 mW m^{-2} nm^{-1} sr^{-1}, SZA = 20°, and nadir as a function of surface albedo for different instrument spectral resolutions.

AMTD
5, 163–210, 2012

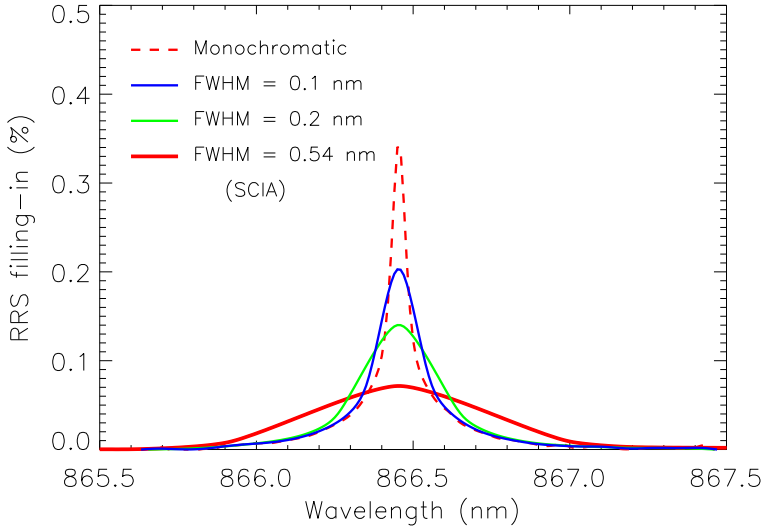

Fig. 4. Simulated filling-in spectra due to rotational-Raman scattering (RRS) only at SZA = 40°, nadir, and surface albedo=0.3 for different instrument spectral resolutions.

AMTD
5, 163–210, 2012

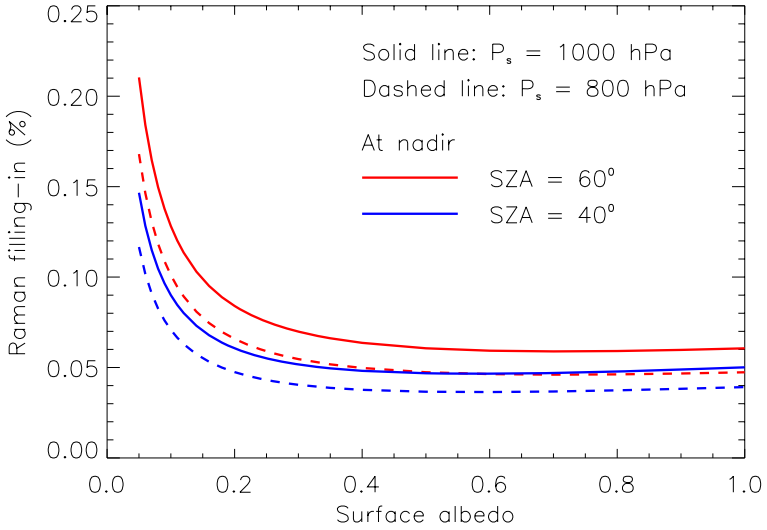

Fig. 5. Filling-in of Ca II line at 866 nm due to rotational-Raman scattering as a function of surface albedo for two solar zenith angles (SZA) and two surface pressures (P_s) showing simulated difference between low clouds over ocean (800 hPa) and a low lying land area (1000 hPa).

AMTD
5, 163–210, 2012

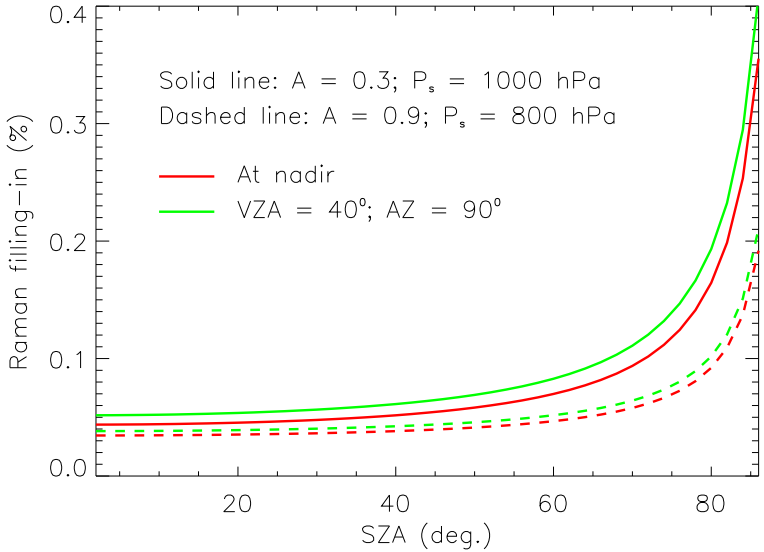

Fig. 6. Filling-in of Ca II line at 866 nm due to rotational-Raman scattering as a function of solar zenith angle (SZA) for 2 view zenith angles (VZA) typical of minimum (nadir, 0°) and maximum (40°) for SCIAMACHY for a relative azimuth angle (AZ) of 90°.

AMTD
5, 163–210, 2012

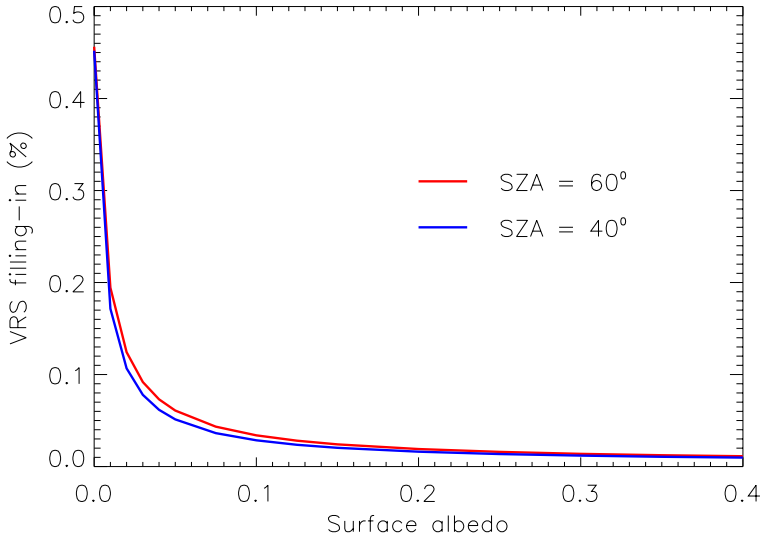

Fig. 7. Filling-in of Ca II line at 866 nm due to vibrational-Raman scattering (VRS) as a function of surface albedo for 2 solar zenith angles (SZA).

AMTD
5, 163–210, 2012

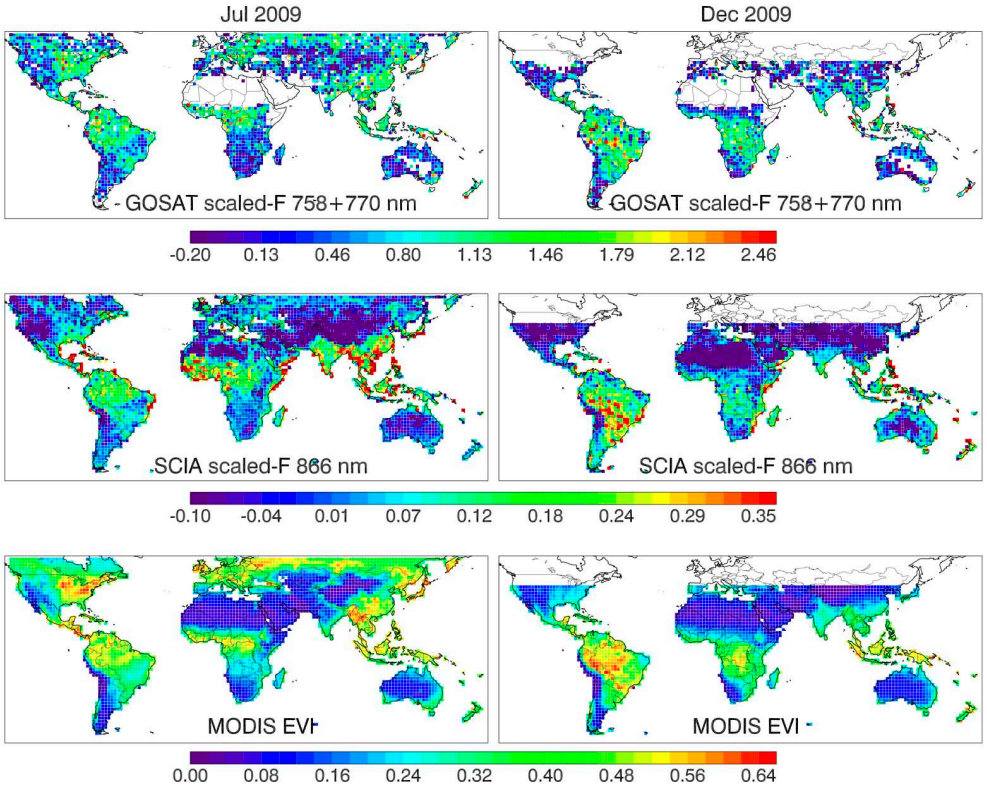

Fig. 8. Derived monthly averages for July (left panels) and December (right panels) 2009; Top: fluorescence scaled by cos(SZA) (scaled-F) (unitless) from GOSAT (0.696*758 nm + 770 nm); Middle SCIAMACHY 866 nm; Bottom: Aqua MODIS enhanced vegetation index (EVI)

AMTD
5, 163–210, 2012

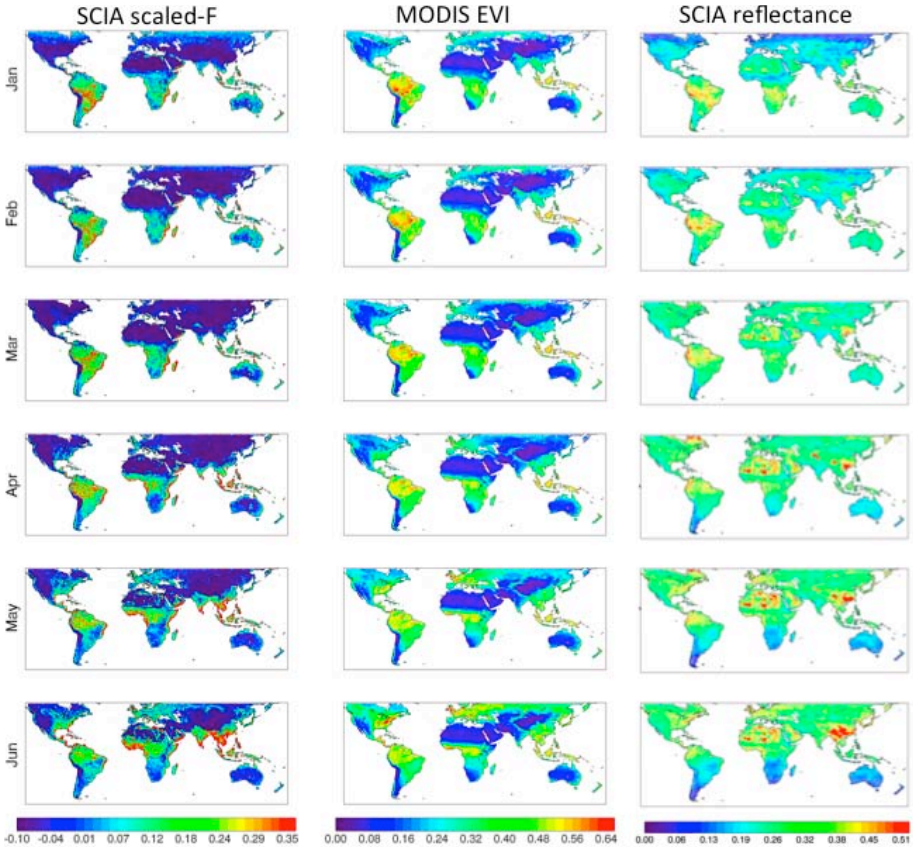

Fig. 9. Monthly mean scaled-F (left) and reflectance (right) derived from 8+ yr of SCIAMACHY data gridded at $0.5^{\circ} \times 0.5^{\circ}$ resolution and gridded EVI from 9 yr of Aqua MODIS at the same spatial resolution (middle) for January through June (top to bottom).

AMTD
5, 163–210, 2012

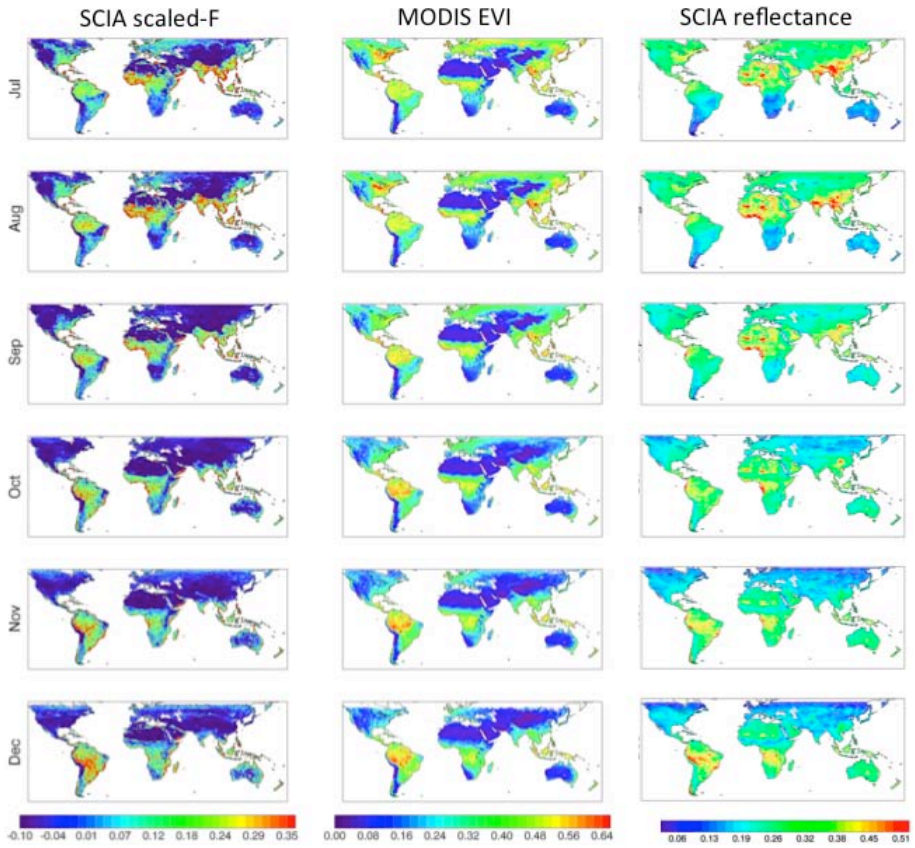

Fig. 10. Similar to Fig. 9 but for July through December.

AMTD
5, 163–210, 2012

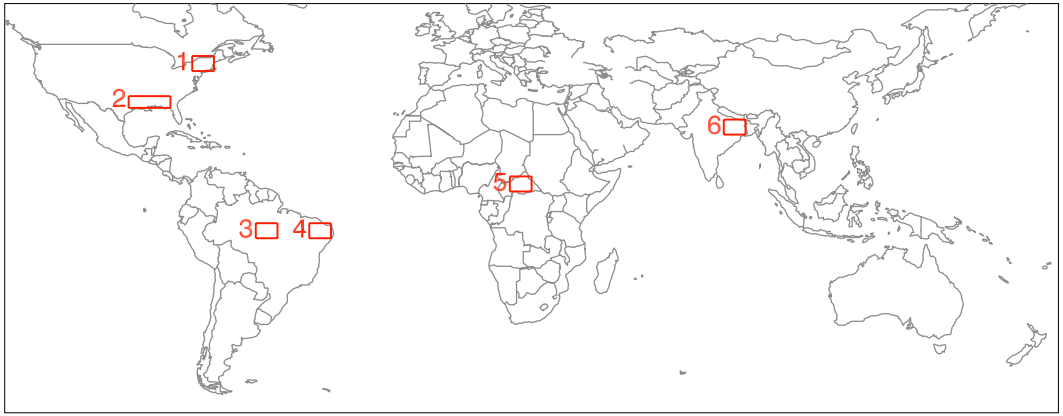

Fig. 11. Regions used for calculating seasonal cycles shown in Fig. 12.

AMTD
5, 163–210, 2012

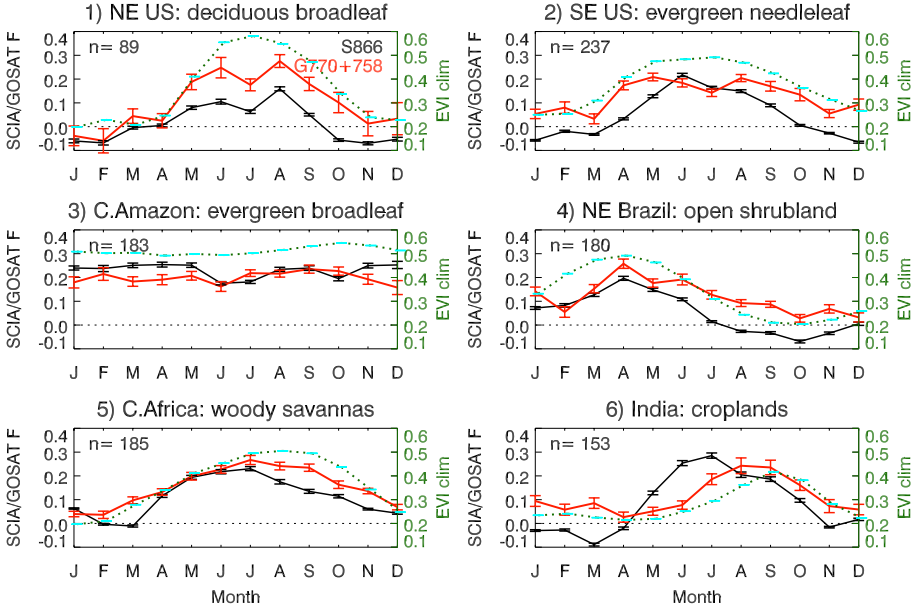

Fig. 12. Seasonal cycles derived for the regions shown in the Fig. 11 map, using 0.5° × 0.5° gridbox monthly means within the region and with the dominant vegetation type as listed: Black solid line: scaled-F derived from SCIAMACHY (left axis, unitless) and scaled GOSAT (combined 758 and 770 nm divided by 6, red); vertical bars indicate error of the mean Green dotted line: MODIS Enhanced Vegetation Index (EVI, right axis, unitless). The numbers indicated are the number of monthly mean 0.5° × 0.5° gridboxes used in each plot.

AMTD
5, 163–210, 2012